Wakefield in solid state plasma with the ionic lattice force

Sahel Hakimi, Tam Nguyen, Deano Farinella, Calvin K. Lau, Hsuan-Yu Wang, Peter Taborek, Franklin Dollar, and Toshiki Tajima

Citation: Physics of Plasmas **25**, 023112 (2018); doi: 10.1063/1.5016445
View online: https://doi.org/10.1063/1.5016445
View Table of Contents: http://aip.scitation.org/toc/php/25/2
Published by the American Institute of Physics

Wakefield in solid state plasma with the ionic lattice force

Sahel Hakimi,[a] Tam Nguyen, Deano Farinella, Calvin K. Lau, Hsuan-Yu Wang, Peter Taborek, Franklin Dollar, and Toshiki Tajima
Department of Physics and Astronomy, University of California, Irvine, California 92697, USA

(Received 19 November 2017; accepted 6 February 2018; published online 26 February 2018)

The advent of the path to a single cycle X-ray laser pulse via thin film compression and the relativistic compression enables laser wakefield acceleration in solid materials. We study the collective interaction of the X-ray laser pulse with the solid-state plasma, including ultrafast polariton effects, giving rise to TeV/cm wakefields with highly increased critical density. Our particle-in-cell computational analysis delineates wakefield effects and polariton dynamics. We show that a good quality wakefield can be excited even in the presence of the lattice force and the electron acceleration process is not influenced by polaritons. The applications and implications of the ultrafast wakefield and ultrafast plasmonics are discussed. *Published by AIP Publishing.*
https://doi.org/10.1063/1.5016445

I. INTRODUCTION

The present work is motivated by the recent invention of the Thin Film Compression technique[1] for lasers, which enables the compression of an intense laser. This leads to a realization of the relativistic compression of such a pulse into an X-ray laser pulse.[2]

Traditional particle acceleration technology uses excited radiofrequency (RF) waves in vacuum surrounded by metal or dielectric waveguides and has an acceleration gradient limit of approximately 1 MeV/cm due to material breakdown. Thus, larger and more expensive accelerator facilities are necessary in order to obtain higher energy particle beams. The alternative technique of laser wakefield acceleration (LWFA) uses plasma as the accelerating medium and is capable of producing acceleration gradients three orders of magnitude higher compared to traditional accelerators since plasma does not suffer material breakdown and can sustain very large electric fields.[3,4] More details on laser-driven plasma-based accelerators can be found in previously published review papers.[5–8] In LWFA, the ponderomotive (or radiation pressure) force of an intense laser pulse with the appropriate length moving through an under-dense plasma causes electrons to oscillate at the plasma frequency, $\omega_{pe} \propto \sqrt{n_e}$, and excites a plasma wave (plasmon) that co-moves with the laser pulse. Electrons trapped in this robust structure can acquire relativistic energies. Electron energy gain in 1D LWFA is given by

$$\epsilon = 2a_0^2 m_e c^2 \left(\frac{n_{cr}}{n_e}\right), \tag{1}$$

where $a_0 = eE_0/m_e\omega_l c$ is the normalized vector potential of the laser pulse with E_0 and ω_l representing the electric field and frequency of the laser. Here, e, m_e, and c are the electron charge, electron mass, and speed of light, respectively. The energy gain is proportional to the ratio of n_{cr}, critical density defined by the laser frequency, to n_e, the plasma or electron density. According to the above equation, the energy gain of particles is inversely proportional to the plasma density. Thus far, increasing the energy gain has been carried out by decreasing the plasma density. However, the acceleration length is given by

$$L_{acc} = a_0 \left(\frac{c}{\omega_{pe}}\right)\left(\frac{\omega_l}{\omega_{pe}}\right)^2 \propto \left(\frac{n_{cr}}{n_e^{3/2}}\right). \tag{2}$$

Hence, the acceleration length is inversely proportional to $n_e^{3/2}$ and will increase as well when n_e is decreased, an inconvenient outcome when attempting to increase the energy gain according to Eq. (1). Furthermore, when n_e is decreased, it is necessary to increase the laser energy as the volume occupied by the laser pulse increases proportional to the plasma skin depth, $(c/\omega_{pe})^3$.[2,4]

Alternatively, energy gain may be achieved without decreasing the plasma density or even under the appropriate increase in density, making higher acceleration gradients possible within more compact structures. This is possible by increasing n_{cr} through increasing the laser frequency. The introduction of a technology to make X-ray lasers (over optical lasers) can accomplish this. For current optical lasers and gaseous plasmas, the typical ratio is $n_{cr}/n_e = 10^{21}\,\mathrm{cm}^{-3}/10^{18}\,\mathrm{cm}^{-3} = 10^3$, whereas for an X-ray laser and a solid density plasma, we could for example have $n_{cr}/n_e = 10^{29}\,\mathrm{cm}^{-3}/10^{23}\,\mathrm{cm}^{-3} = 10^6$, three orders of magnitude higher. To X-ray photons with keV energies, shallowly bound electrons are effectively free electrons and the electron motion may be regarded as plasma-like in the timescale of the X-ray pulse, while more strongly bound electrons remain intact. The solid material is not ionized during the interaction as the timescale for the above threshold ionization is long compared to the attosecond timescale of the X-ray photons. Electrons oscillate a relatively small distance about their original location to produce the wakefield. If the wakefield reaches on the order of the Tajima-Dawson field,[4] some electrons will get ripped from the atoms and will be accelerated. Furthermore, when we inject electrons into this structure in a control manner, the produced wakefield accelerates the injected electrons. In order to minimize collisions between the accelerated electrons within the wake structure and the electrons

[a]sahelh@uci.edu

from the solid, it is suggested to use fabricated nanotubes,[9–12] and after the passing of the X-ray pulse, one could choose a different nanotube if needed.

Although X-ray acceleration had been considered prior to this,[13] the prospect for an adequate laser driver did not exist. Recently, the advancement of laser technology through Thin Film Compression (TFC)[1] has made X-ray pulse generation achievable with an optical laser in the single cycle regime. The relativistic compression method for conversion into the X-ray regime can then be employed.[2] This combination, if realized, allows both single cycle X-ray lasers and intense regimes. TFC introduces a thin film of material such as plastic in the path of the beam to broaden its frequency bandwidth by the self-phase modulation. The beam is then compressed by chirped mirrors to its fundamental single cycle regime with nearly 10 times higher peak power. The upconversion of this single cycle optical pulse to an X-ray pulse via compression processes in an over-critical solid target[2] provides an intense X-ray laser pulse. We note that single or sub-cyclic laser pulses have been realized in attosecond science (although not intense).[14,15] Also, we note that the sub-cyclic particle accelerator has been explored.[16]

These new advancements allow us to consider LWFA in the X-ray regime and with solid densities.[13,17–19] High energy X-ray photons can directly interact with free charged particles or electrons in the outer shells as if they are unbound or weakly bound electrons; therefore, solid materials such as dielectrics or metals can be regarded as metallic plasmas at solid densities as the intense ultrashort X-ray laser passes through. Meanwhile, such an X-ray laser pulse can couple with ionic motions through optical phonon modes as will be discussed below. Recently, Zhang *et al.* studied the LWFA driven by an X-ray laser in a solid density nanotube and found the LWFA scalings.[20] The simulations in that work confirmed an accelerating gradient of TeV/cm when the wakefield is driven by an X-ray laser compared to GeV/cm for when it is driven by an optical laser. However, in that work, the solid state effects (polaritons)[21] have not been included. In this work, we include the effects of ionic motion explicitly and investigate the possibility that the lattice force could couple with the formation of a stable wake structure. We show that wakefield formation and electron acceleration processes are not influenced by the presence of polaritons. The present results indicate the acceleration gradient on the order of TeV/cm, which agrees well with the wakefield theory and is consistent with previous findings without the lattice effect.[20] This amounts to the validation by computation of the concept of the solid state plasma wakefield in nanomaterials.

The present analytical model is based on the dispersion relation of the bulk system of the coupled phonon-plasmon in the solid state. The basic equations for this setup are the continuity and momentum equations for both species and Poisson's equation

$$\frac{\partial n_e}{\partial t} + \nabla \cdot (n_e(v_D + v_e)) = 0, \quad \frac{\partial n_i}{\partial t} + \nabla \cdot (n_i v_i) = 0, \tag{3}$$

$$m_e n_e \left(\frac{\partial v_e}{\partial t} + (v_D + v_e) \cdot \nabla v_e \right) = n_e q_e E - \nabla P_e, \tag{4}$$

$$m_i n_i \left(\frac{\partial v_i}{\partial t} + v_i \cdot \nabla v_i \right) = n_i q_i E - K_i (x_i - x_{i0}), \tag{5}$$

$$\nabla \cdot E = 4\pi e (n_i - n_e), \tag{6}$$

$$\xi_e = \frac{eE}{m_e \omega^2 - m_e k_x v_D \omega - \dfrac{k_x^2 \gamma T_e \omega}{\omega - k_x v_D}}, \tag{7}$$

$$\xi_i = \frac{-eE/m_i}{\omega^2 - \dfrac{K_i}{m_i}}, \tag{8}$$

where v_D, v_e, and v_i are the drift velocity of electrons, thermal velocity of electrons, and thermal velocity of ions, respectively. E and P_e represent the electric field and electron pressure, K_i is the effective spring constant for the lattice force of the neighboring ions, and $\xi_\alpha (\alpha = e, i)$ are the displacements of charged particles. In a 1D framework, we use perturbation theory to write the equivalent 1st order equations and use Fourier theory, assuming $A = A_0 e^{i(kx - \omega t)}$ form for each perturbed quantity, to solve for the perturbed positions. Substituting into Poisson's equation gives the dispersion relation where $\epsilon(k, \omega)$ is the relative permittivity (setting $v_D = 0$)

$$\epsilon(k, \omega) = 1 - \frac{\omega_{pi}^2}{\omega^2 - \omega_{TO}^2} - \frac{\omega_{pe}^2}{\omega^2 - k_x^2 v_e^2}. \tag{9}$$

Therefore, this model is capable of including the important effects of ionic motions such as the polaritons and collective modes at solid densities by including the transverse optical phonon frequency, $\omega_{TO} = \sqrt{K_i/m_i}$, in the dispersion relation.[21] In fact, this model was previously applied to the plasmonic excitations such as plasmons and polaritons in the solid bulk and in the surface of these materials[21–25] driven by a laser or an electron current.

In Sec. II, we provide an overview of the code and the modifications to model ionic motion, explain the initial setup and parameters of the LWFA simulations, and present the results indicating no noticeable deleterious effect or instability arising from the addition of ionic lattice force. In Sec. III, we use this modified code and present simulations of a current driven instability in different regimes of high and low ionic frequencies having distinct behaviors. In Sec. IV, we discuss a few applications related to these findings, and Sec. V contains concluding remarks and a discussion of extension of this work in the future.

II. WAKEFIELD SIMULATIONS

We investigate the LWFA process driven by an X-ray laser onto solid density materials. A 1D simulation of a high frequency laser is performed, which interacts with a high density plasma consisting of free electrons and a lattice of ions that feel the vibrational force from their neighbor ions. We assume an isometric lattice structure and focus on the regime where the laser pulse is within the accelerating region of the wake. We also assume that the laser spot width is far greater than the X-ray pulse length. Therefore, we can perform the simulation and analysis in 1D where the theory and

scaling laws are very well known for the purpose of benchmarking and further analysis. Our first goal is to study the ionic mode in order to see if it has any effects on the wakefield formation or electron acceleration in the longitudinal direction.

A. Introduction of ionic motion at the solid density

Simulations for this work are conducted using the 1D version of the EPOCH particle-in-cell (PIC) code[26] with the second order field solver. EPOCH is a well-benchmarked relativistic electromagnetic PIC code[27,28] which uses the finite-difference time-domain technique to numerically solve Maxwell's equations and the leap-frog method with the Boris algorithm to update the velocities and positions of particles.[29,30]

We modify several subroutines in this code in order to manually load particles in a structured lattice and also include the effects of the lattice force.[31] Major modifications happen in EPOCH's pusher, where velocities of particles are updated, by including the second term in the following equation in order to model the lattice force

$$\frac{d\,\underset{\sim}{v_n}}{dt}\hat{x} = \frac{q}{m}(\underset{\sim}{E} + \underset{\sim}{v_n} \times \underset{\sim}{B})\hat{x} - \frac{K_i}{m}(x_n - x_{n0})\hat{x}, \tag{10}$$

where x_{n0} is the initial position of the particle at $t = 0$ and x_n is its position at the current iteration. This new term only affects the advancement of positive charges, and K_e is set to be zero for negative charges at all times.

The initial setup is composed of ions loaded uniformly into an ordered lattice structure and of particles with negative charge loaded randomly. One positive ion is positioned exactly at the center of each cell, while multiple particles with negative charge, with the appropriate charge (and mass) weight to ensure the overall charge neutrality, are distributed throughout each cell. Plasma density is $n_i = n_e = 10^{23}\,\mathrm{cm}^{-3}$, and $\omega_{pi}/\omega_{pe} = \sqrt{m_e/m_i} \approx 1/43$. Particles are interpolated to the grid using a third order b-spline shape function. The simulation domain is 1D in space ($\hat{x}$-direction) with periodic boundaries at both ends. Each cell is 1 Å in size similar to the average spacing in solids. Temperature is set to zero for both species.

A Gaussian electromagnetic wave-packet, polarized in the y-direction, with a full width half max equal to $\lambda_{pe}/4$ and $a_0 = 3$ is initialized and set to move through the initial plasma setup in the $\hat{x}$-direction; here, $\lambda_{pe} = 2\pi c/\omega_{pe}$ is the plasma wavelength. The carrier frequency of the pulse is 30 PHz ($\lambda_l = 10^{-6}\,\mathrm{cm}$) corresponding to $\approx 125\,\mathrm{eV}$ photons. The ratio of laser frequency to plasma frequency is $\omega_l/\omega_{pe} = \sqrt{n_{cr}/n_e} = 10.5$. We collect data every $\lambda_{pe}/2c$ step until the electron energy saturation is observed. Table I provides a summary of the parameters used in the simulation.

TABLE I. Summary of LWFA simulation parameters.

Plasma density	n_e	10^{23}	cm^{-3}
Laser wavelength	λ_l	10^{-6}	cm
Laser intensity	a_0	3	…
FWHM	$\lambda_{pe}/4$	2.65×10^{-6}	cm
Grid size	δx	10^{-8}	cm
δt	$\delta x/0.95c$	3.5×10^{-19}	s

B. X-ray laser wakefield excitation in the solid

We conduct simulations with the specified parameters for several different values of effective spring constant. The initial simulation sets $K_i = 0$ and is predicted to show a typical wakefield evolution. We benchmark the modified code by comparing the result from this run with another simulation conducted using the original code where lattice force was not yet introduced. Figure 1 shows the results from this initial run. We show the laser pulse as it travels through the plasma and the wakefield structure that forms behind it (longitudinal electric field) at times $5\lambda_{pe}/c = 1.76$ fs, $9\lambda_{pe}/c = 3.17$ fs, and $11.5\lambda_{pe}/c = 4.05$ fs. Phase space is also shown for both species. Electric fields E_x and E_y are normalized by the Tajima-Dawson field[4] $E_L^{cr} = m_e\omega_{pe}c/e$, the momentum is normalized by $m_e c$, and the position is normalized by λ_{pe}. As the pulse moves through the plasma, it pushes electrons out of its way and creates a region with positive charges; this region is approximately $\lambda_{pe}\sqrt{a_0}$ wide as seen in Fig. 1. The excited longitudinal electric field is seen to attain amplitude on the order of E_L^{cr}, consistent with the theory. This electric field results in an accelerating gradient of $eE_L \approx 1.4eE_L^{cr} \approx 0.4\,\mathrm{TeV/cm}$ in the wakefield, which matches the theoretical prediction of $eE_L^{cr} = 0.3\,\mathrm{TeV/cm}$. It is shown that electrons at the end of each bubble continue to gain energy as the wakefield evolves and the pulse moves through the plasma. This is the limit of the plasma wave (plasmon) dominated regime of the collective modes in the solid state plasma. The observed electron energy gain [even for the case of $\omega_{pe} < \omega_{TO}$, shown in Figs. 2(e) and 2(f)] is $\epsilon \approx 100 m_e c^2 \approx 50\,\mathrm{MeV}$, while the 1D LWFA theory predicts the maximum energy gain of $\approx 900\,\mathrm{MeV}$. The maximum electron energy is observed to be $\approx 340\,\mathrm{MeV}$ in later stages of the simulation and is limited by the pump depletion length.

We then vary the strength of the lattice force by changing the effective spring constant. Table II summarizes different ratios we use to simulate these distinct cases. Figure 2 shows the result of several simulations when transverse optical phonon frequency is less than, equal to, and greater than electron plasma frequency. We show the result of each simulation at $t = 11.5\lambda_{pe}/c = 4.05$ fs. These figures can also be compared with Figs. 1(e) and 1(f), corresponding to the case of $\omega_{TO}/\omega_{pe} = 0$ at this exact time. It is observed that the wakefield or longitudinal electric field is not affected by the presence of ion modes and negative charges bunched at the end of each bubble continue to gain momentum and energy comparable to the base case with $K_i = 0$. A noticeable difference in these cases compared to the base case is the presence of an ion mode related to the lattice frequency, but the fundamentals of the LWFA are unaffected. Thus, we show that the basic wakefield (plasmons excited by the mechanism of the wakefield[4]) is only slightly affected by the size of ω_{TO}/ω_{pe}.

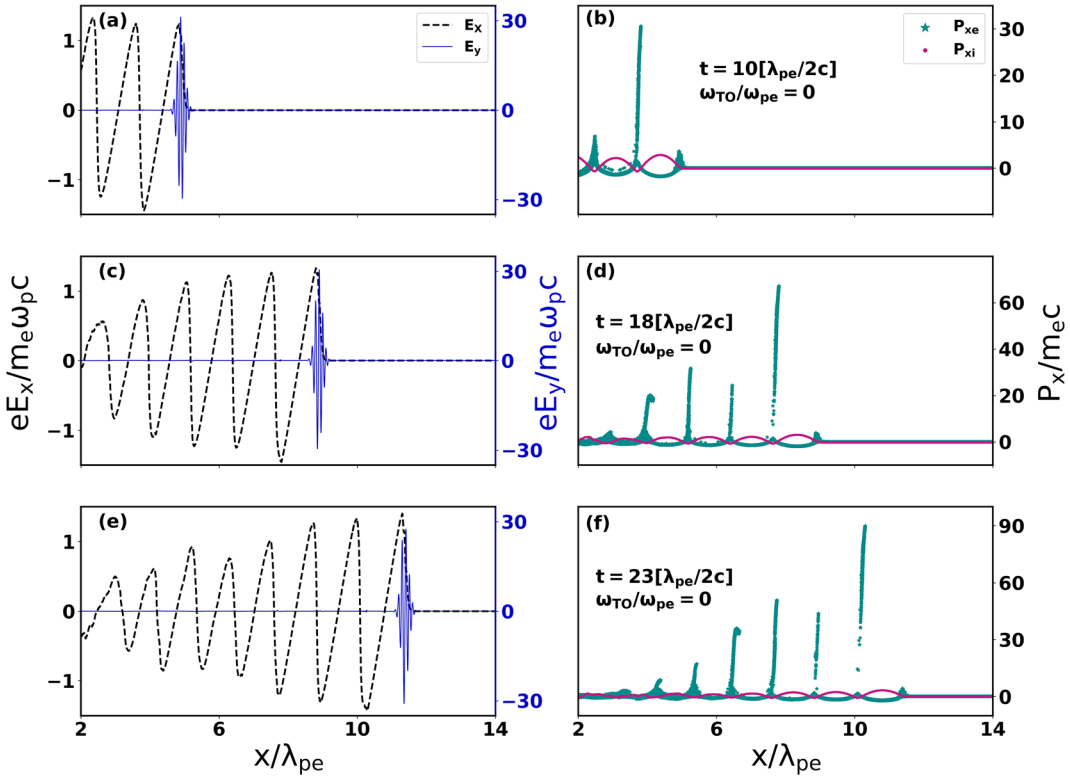

FIG. 1. Evolution of LWFA with $\omega_{TO}=0$ at $t/[\lambda_{pe}/2c]=10$ [panels (a) and (b)], $t/[\lambda_{pe}/2c]=18$ [panels (c) and (d)], and $t/[\lambda_{pe}/2c]=23$ [panels (e) and (f)] is shown. Panels (a), (c), and (e) show the electric field of the laser pulse, E_y, shown by the blue solid line (right axis) and longitudinal electric field, E_x, shown by the black dashed line (left axis) normalized by E_L^{cr}. Panels (b), (d), and (f) show the phase space for each species. Green stars represent simulation particles with negative charge, and red dots represent simulation particles with positive charge. The momentum (right axis) is normalized by m_ec, and the position is normalized by λ_{pe}.

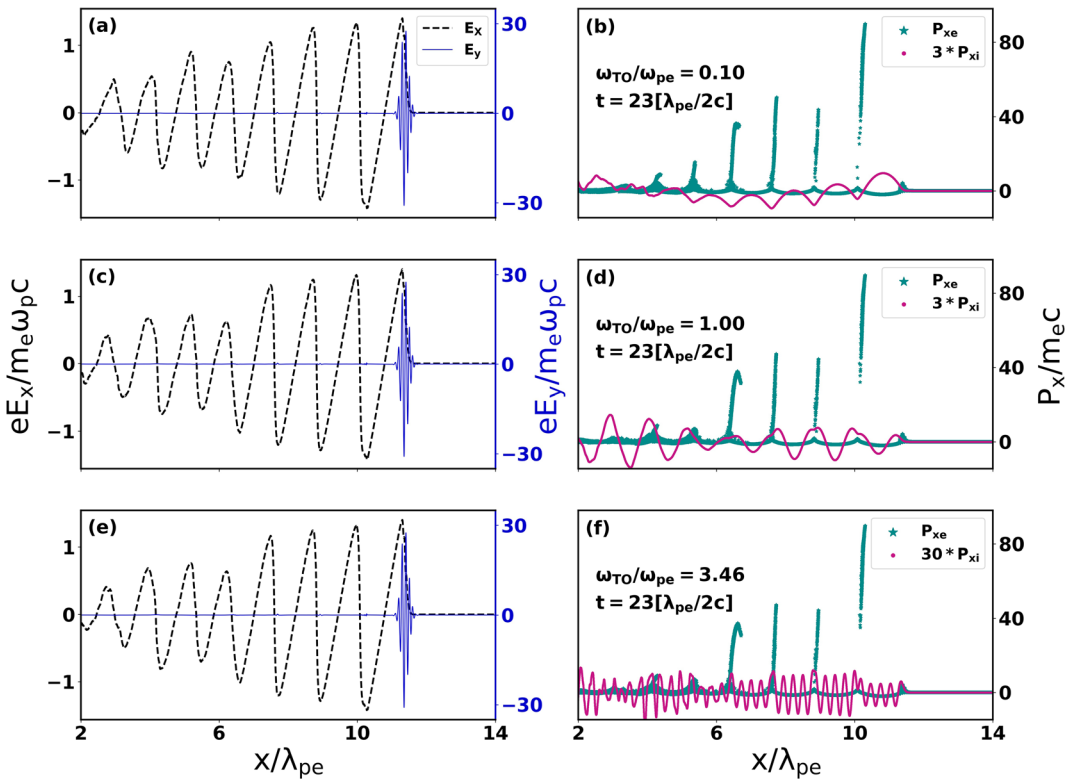

FIG. 2. Comparison of different lattice force strengths is shown at $t/[\lambda_{pe}/2c]=23$ for $\omega_{TO}/\omega_{pe}=0.10$ [panels (a) and (b)], $\omega_{TO}/\omega_{pe}=1$ [panels (c) and (d)], and $\omega_{TO}/\omega_{pe}=3.46$ [panels (e) and (f)]. Organization and normalization are the same as described in Fig. 1, while the amplitude of the ion mode is increased [by a factor of 3 in panels (b) and (d) and by a factor of 30 in panel (f)] with the intention to display it clearly.

TABLE II. Different cases of LWFA simulation.

Case	$\frac{\omega_{pi}}{\omega_{pe}}$	$\frac{\omega_{TO}}{\omega_{pe}}$
1	1/43	0
2	1/43	0.10
3	1/43	1
4	1/43	3.46

This is thus consistent with the earlier model of the wakefield formation through solid densities.[20]

III. SIMULATION OF BEAM-DRIVEN INSTABILITIES

Similar plasmons and polaritons (electron plasma waves and ionic plasma modes) can be excited in a solid plasma system with the presence of an electron current. The dispersion relations of the bulk modes with current and surface polaritons have been studied previously.[21] We confirm the existence of the bulk mode excitation via simulations using the same modified PIC code as above. More information on the theory behind these modes can be found in references such as Refs. 22–24 and 31. If we assume that electrons have a constant drift velocity and move through a 1D lattice of ions, Eq. (9) will be slightly modified to[21]

$$\epsilon(k,\omega) = 1 - \frac{\omega_{pi}^2}{\omega^2 - \omega_{TO}^2} - \frac{\omega_{pe}^2}{(\omega - k_x v_D^2)^2 - k_x^2 v_e^2}. \quad (11)$$

The initial setup for the simulation is similar to Sec. II. Positive ions are manually positioned at the center of each cell, while negative charges are loaded randomly throughout each cell. The plasma density is slightly higher, $n_i = n_e = 10^{24}\,\mathrm{cm}^{-3}$. The simulation window is 450 Å wide with 450 cells. The temperature is set to zero for both species. The electron drift velocity is varied, but in this paper, we present the results for the case of $v_D = c/2$. The modified code was also benchmarked against the well-known Buneman case when $K_i = 0$. Here, we show simulation results from two distinct cases with different sets of parameters as summarized in Table III.

A. High ionic frequency modes (polariton)

Equation (11) has four different solutions, two of which may be complex conjugate solutions with one unstable solution. In the first case, we study the ratio of $\omega_{pi}/\omega_{pe} = 1/2$ and $\omega_{TO}/\omega_{pe} = 3.46$. This means that the frequency of the transverse optical phonon is much greater than that of the plasmon. This is a low density regime, and polaritons are destabilized in this regime. All four solutions of the linear dispersion relation with these specified parameters are plotted in Fig. 3 using a polynomial solver. The real frequency versus the wavevector is shown in Fig. 3(a), and the growth rate versus the wavevector is shown in Fig. 3(b). The real frequency and growth rate are normalized by ω_{pe}, and the wavevector is normalized by ω_{pe}/c. The top and bottom branches are phonon-like branches in the positive and negative frequencies. The middle two branches are plasmon-like in the lower wavevector range. The instability is due to the charge bunching mechanism and occurs when the forward propagating phonon branch meets the negative energy plasmon wave.[21] The unstable wave has wavelength $\lambda = 2\pi/k = 37 \times 10^{-8}\,\mathrm{cm}$, where $k = 4.46\omega_{pe}/0.5c = 8.9\omega_{pe}/c$ as seen in Fig. 3(a). Figure 4 displays the result of the simulation, studying their nonlinear behavior, with the observed wavelength of the unstable mode being $35 \times 10^{-8}\,\mathrm{cm}$ matching the predicted wavelength (within 5 percent). The measured growth rate for this mode matches the dispersion relation solution and is marked in Fig. 3(b). The growth rate is measured from the slope of the logarithm of a Fourier component of the electric field in time. We show the evolution of this instability and the growth of this mode into a nonlinear phase. We observe that the instability picks up growing linearly [Fig. 4(b)] and eventually is nonlinearly modulated to form trapped electron orbital characteristic [Fig. 4(c)], while ions display a more harmonic behavior throughout. In the latest nonlinear stage [Fig. 4(d)], electrons show nearly closed trapped orbitals. The electron nonlinearities are similar to gas plasma electron dynamics (with less chaotic elements), but ions do show a more harmonic behavior. At the saturation [Fig. 4(c)], the acceleration gradient is $eE_x \sim 0.1eE_L^{cr} \approx 100\mathrm{GeV/cm}$ at $t = 1.2$ fs.

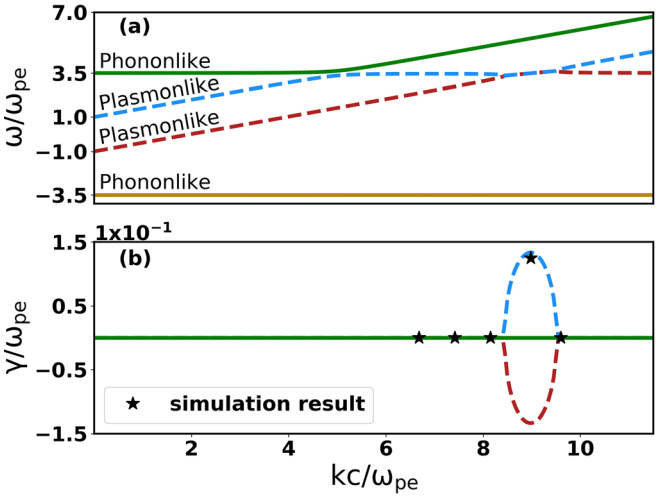

FIG. 3. Dispersion relation of the bulk modes with current (low density case). $\omega_{pi}/\omega_{pe} = 0.5$ and $\omega_{TO}/\omega_{pe} = 3.46$, $v_D = 0.5c$. Panel (a) shows the normalized real frequency, ω/ω_{pe}, vs. normalized wavevector, kc/ω_{pe}. The top and bottom branches are phonon-like, and the two middle branches are plasmon-like at lower wavevectors. The instability occurs when the forward propagating phonon branch crosses the negative energy plasmon branch. Panel (b) shows the normalized growth rate, γ/ω_{pe}, vs. normalized wavevector. The stars mark the values of the growth rate found from the simulation data for several modes.

TABLE III. Different cases of beam-driven instability simulation.

Case	$\frac{\omega_{pi}}{\omega_{pe}}$	$\frac{\omega_{TO}}{\omega_{pe}}$
High ionic frequency	1/2	3.46
Low ionic frequency	1/63	0.11

B. Low ionic frequency modes (polariton)

In the second case, we study the ratio of $\omega_{pi}/\omega_{pe} = 1/63$ and $\omega_{TO}/\omega_{pe} = 0.11$. This is a high density regime. Solutions

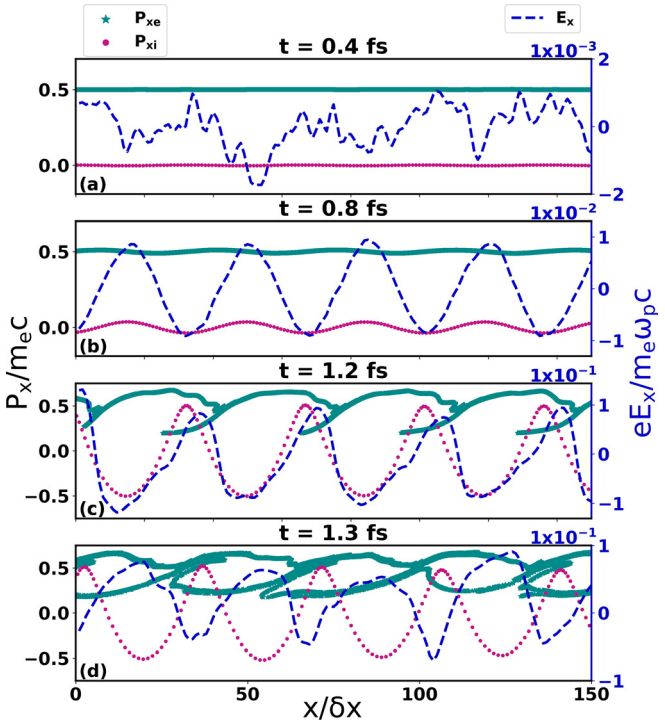

FIG. 4. Time evolution of the unstable mode from simulation data for the case of high ionic frequency is shown. Phase space for each species is shown where momentum is normalized by $m_e c$ plotted on the left axis. The horizontal axis shows the position of particles in the simulation window normalized by the simulation grid size, 1 Å. Green stars represent simulation particles with negative charge, and red dots represent simulation particles with positive charge. The blue dashed line represent the longitudinal electric field plotted on the right axis and normalized by E_L^{cr}.

of the dispersion relation with these parameters are plotted in Fig. 5. The real frequency versus the wavevector is shown in Fig. 5(a), and the growth rate versus the wavevector is shown in Fig. 5(b). Normalization is the same as the previous case. In these plots, the top and bottom branches are plasmon-like, and the middle two branches are phonon-like in the lower wavevector range. The instability is again due to charge bunching and occurs at the crossing of the optical phonon and the negative energy plasmon branch. The unstable wave has wavelength $\lambda = 2\pi/k = 152 \times 10^{-8}$ cm, where $k = 1.1\omega_{pe}/0.5c = 2.2\omega_{pe}/c$ as seen in Fig. 5(a). The simulation result [Fig. 6] shows the observed wavelength of the unstable mode having $\lambda = 150 \times 10^{-8}$ cm matching the predicted wavelength (within 2 percent), and the measured growth rate is on the same order of magnitude as Eq. (11) suggests, marked in Fig. 5(b). We show the evolution of this mode; however, this instability is so weak that we observe no electron trapping phenomena similar to what have been observed in Fig. 4 or in the laser wakefield case [Figs. 1 and 2]. Simulations for both cases were conducted with varying velocities including lower velocities, for example, $v_D = 0.07c$, showing the same typical results as discussed here.

IV. APPLICATIONS

These X-ray driven wakefield accelerators at the solid density have been considered for future high energy

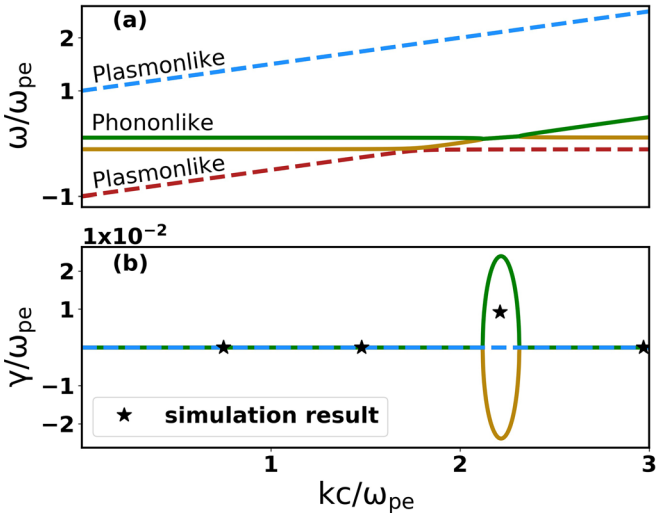

FIG. 5. Dispersion relation of the bulk modes with current (high density case). $\omega_{pi}/\omega_{pe} = 0.016$, $\omega_{TO}/\omega_{pe} = 0.11$, and $v_D = 0.5c$. Panel (a) shows the normalized real frequency, ω/ω_{pe}, vs. normalized wavevector, kc/ω_{pe}. The top and bottom branches are plasmon-like, and the two middle branches are phonon-like at lower wavevectors. The instability occurs when the forward propagating phonon branch crosses the negative energy plasmon branch. Panel (b) shows the normalized growth rate, γ/ω_{pe}, vs. normalized wavevector. The stars mark the values of the growth rate found from the simulation data for several modes.

accelerators for electrons and perhaps ions.[17,18] These works are further extensions of the laser wakefield toward future high energy electron accelerators;[32–39] however, for the application to a high energy electron accelerator,[6] we suggested the adoption of nanotube materials to avoid high energy electrons scattering from the electrons in the solid, by

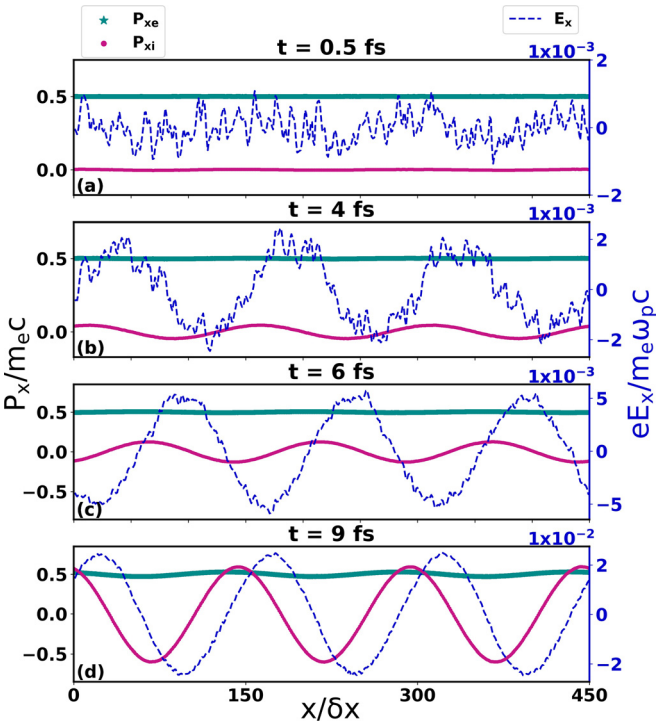

FIG. 6. Time evolution of the unstable mode from simulation data for the case of low ionic frequency is shown. Organization and normalization are the same as described in Fig. 4.

creating a concave hole of much lower electron density in the nanotube.[40–42] Using solid materials has the advantage of being compact and designable for controlled acceleration. Zhang *et al*. have shown that the wakefield in a nanotube is reasonable for the acceleration.[20] In fact, the nanotube wakefield is more ideal as its transverse structure confines the laser energy and is more regulated, and subsequent betatron motions are cleaner and thus provide superior beam quality.[20] In addition, the nanotube structure is great for guiding and the repetitive honeycomb structure of these materials such as alumina nanotubes makes it possible to raster repetitive pulse injection. It is evident that the present X-ray acceleration regime has far higher accelerating gradients than that of the dielectric X-ray acceleration,[43] this is because the present X-ray can operate in the "plasma regime" (i.e., above the ionization fields).

Furthermore, we note that the timescale of the present ultrafast X-ray pulse (nearly one-cycle regime) and its interaction with the plasmon (at the solid density) wakefield immediately following the laser pulse happens in a matter of hundreds of attoseconds. The above field ionization and subsequent lattice movement time scales (such as potential melting) are far longer than the physics we have discussed.[44] There is also a possibility of atom stabilization due to the rapid laser oscillations.[45] The nanotube structure may not even be damaged and could be used multiple times. When a particular nanohole is damaged, we can raster the laser injection to the adjacent holes.

The plasmon and polariton excitations in such a solid state material by either an X-ray laser or drifting electrons should be of interest to recent plasmonic applications.[46–50] There is also interest to use X-ray lasers as probes to time resolve surface features in plasmonics.[51,52] Previous studies such as Refs. 22–25 laid the foundation of these developments. Particularly, the surface excitations[21] may be applicable to these modes and their localized and controlled excitation with high intensity and ultrafast time scales. The surface wake excitation in the above nanotube is also related to the surface mode excitation and to the dielectric wakefield accelerator scheme.[53,54] Their applications to bioinspired nanomaterials (such as nanocapillaries)[10,55–58] may also be of interest for our future investigations of excitation and monitoring of ultrafast modes in bioinspired nanocapillaries, if these modes may be signals to diagnose what is happening.

V. CONCLUSION

We have carried out simulations and analysis of an X-ray laser pulse interacting with solid state media to elucidate the wakefield excitation process in this novel regime. This is an extension of a previous suggestion[17] and the earlier simulation[20] by explicitly including the ionic motion in these solid state materials. The present work validates the earlier work[20] by showing that the central wakefield dynamics has not been altered by adding the ionic kinematics in terms of the wakefield of interest. In addition, we have also investigated the collective modes associated with these ionic dynamics such as polaritons and its surface analogue modes,[21] which may be excited either by a laser or by an electron current. The new laser compression technique[1] along with the relativistic laser compression technique[2] introduced this regime[17,59] of wakefield acceleration far more realistic than earlier times.[13,40–42] A similar concept in wakefield acceleration in nanomaterials driven by beams has also been suggested.[59,60] We have shown that such an X-ray pulse, if realized by TFC and the relativistic compression technique, can in fact excite good quality LWF, and this is true even in the presence of the lattice force. Once we enter this regime, of attosecond X-ray laser pulses, we anticipate the discovery of the modes of the collective motion coupled with the laser. We can accordingly manipulate these modes with such a laser pulse in a novel way.

The future high energy accelerator applications using nanocapillaries driven by an X-ray laser pulse may become an attractive possibility. The developments should also open up new applications to plasmonics and bioinspired nanomaterial research. We plan to investigate 2D effects in our future research to focus on these effects.

ACKNOWLEDGMENTS

We would like to thank Dr. Ales Necas from Tri Alpha Energy for computational advice and Dr. Young-Min Shin and Dr. Vladimir Shiltsev from Fermilab for insightful discussions. This work was originated from a student term project of the "Plasma Physics" course (PHYSICS 239B) in the 2016 fall quarter at UC Irvine. This work was partially supported by Rostoker fund.

[1]G. Mourou, S. Mironov, E. Khazanov, and A. Sergeev, Eur. Phys. J. Spec. Top. **223**, 1181 (2014).
[2]N. M. Naumova, J. A. Nees, I. V. Sokolov, B. Hou, and G. A. Mourou, Phys. Rev. Lett. **92**, 063902 (2004).
[3]V. A. Veksler, At. Energy **1**, 77 (1956).
[4]T. Tajima and J. M. Dawson, Phys. Rev. Lett. **43**, 267 (1979).
[5]T. Tajima, Proc. Jpn. Acad., Ser. B **86**, 147 (2010).
[6]T. Tajima, K. Nakajima, and G. Mourou, Nuovo Cimento Riv. Ser. **40**, 33 (2017).
[7]G. Mourou, T. Tajima, and S. V. Bulanov, Rev. Mod. Phys. **78**, 309 (2006).
[8]E. Esarey, C. B. Schroeder, and W. P. Leemans, Rev. Mod. Phys. **81**, 1229 (2009).
[9]N. V. Myung, J. Lim, J. P. Fleurial, M. Yun, W. West, and D. Choi, Nanotechnology **15**, 833 (2004).
[10]R. J. Lazarowich, P. Taborek, B.-Y. Yoo, and N. V. Myung, J. Appl. Phys. **101**, 104909 (2007).
[11]P. X. Hou, C. Liu, C. Shi, and H. M. Cheng, Chin. Sci. Bull. **57**, 187 (2012).
[12]M. M. Shulaker, G. Hills, N. Patil, H. Wei, H. Chen, H.-S. P. Wong, and S. Mitra, Nature **501**, 526 (2013).
[13]T. Tajima and M. Cavenago, Phys. Rev. Lett. **59**, 1440 (1987).
[14]M. Hassan, A. Wirth, I. Grguras, T. T. Luu, A. Moulet, V. Yakovlev, J. Gagnon, O. Razskazovskaya, R. Santra, S. Pabst, A. M. Azzeer, Z. A. Alahmed, V. Pervak, F. Krausz, and E. Goulielmakis, in *Laser Science* (Optical Society of America, 2012), pp. LW4H–LW42.
[15]A. Wirth, M. T. Hassan, I. Grguraš, J. Gagnon, A. Moulet, T. T. Luu, S. Pabst, R. Santra, Z. Alahmed, A. Azzeer, V. S. Yakovlev1, V. Pervak, F. Krausz, and E. Goulielmakis, Science **334**, 195 (2011).
[16]B. Rau, T. Tajima, and H. Hojo, Phys. Rev. Lett. **78**, 3310 (1997).
[17]T. Tajima, Eur. Phys. J. Spec. Top. **223**, 1037 (2014).
[18]M. L. Zhou, X. Q. Yan, G. Mourou, J. A. Wheeler, J. H. Bin, J. Schreiber, and T. Tajima, Phys. Plasmas **23**, 043112 (2016).
[19]J. Wheeler, G. Mourou, and T. Tajima, Rev. Accel. Sci. Technol. **9**, 151 (2016).

[20]X. Zhang, T. Tajima, D. Farinella, S. Youngmin, G. Mourou, J. Wheeler, P. Taborek, P. S. Chen, F. Dollar, and B. Shen, Phys. Rev. Accel. Beams **19**, 101004 (2016).
[21]T. Tajima and S. Ushioda, Phys. Rev. B **18**, 1892 (1978).
[22]R. F. Wallis and J. J. Brion, Solid State Commun. **9**, 2099 (1971).
[23]A. Mooradian and A. L. McWhorter, Phys. Rev. Lett. **19**, 849 (1967).
[24]A. A. Maradudin and D. L. Mills, Phys. Rev. B **7**, 2787 (1973).
[25]E. G. Martin, A. A. Maradudin, and R. F. Wallis, Surf. Sci. **91**, 37 (1980).
[26]T. D. Arber, K. Bennett, C. S. Brady, A. Lawrence-Douglas, M. G. Ramsay, N. J. Sircombe, P. Gillies, R. G. Evans, H. Schmitz, A. R. Bell *et al.*, Plasma Phys. Controlled Fusion **57**, 113001 (2015).
[27]T. Tajima, *Computational Plasma Physics with Applications to Fusion and Astrophysics*, Frontiers in Physics Vol. 72 (Westview Press, 1989).
[28]C. K. Birdsall and A. B. Langdon, *Plasma Physics via Computer Simulation* (CRC Press, 2004).
[29]H. Wu, "JPIC & How to make a PIC code," preprint arXiv:1104.3163 (2011).
[30]H. Ruhl, *Classical Particle Simulations with the PSC Code* (Ruhr-Universität Bochum, 2005).
[31]C. Kittel, *Introduction to Solid State Physics* (Wiley, 2005).
[32]K. Nakajima, Light: Sci. Appl. **6**, e17063 (2017).
[33]C. G. R. Geddes, C. Toth, J. Van Tilborg, E. Esarey, C. B. Schroeder, D. Bruhwiler, C. Nieter, J. Cary, and W. P. Leemans, Nature **431**, 538 (2004).
[34]D. Guénot, D. Gustas, A. Vernier, B. Beaurepaire, F. Böhle, M. Bocoum, M. Lozano, A. Jullien, R. Lopez-Martens, A. Lifschitz *et al.*, Nat. Photonics **11**, 293 (2017).
[35]J. Cowley, C. Thornton, C. Arran, R. J. Shalloo, L. Corner, G. Cheung, C. D. Gregory, S. P. D. Mangles, N. H. Matlis, D. R. Symes *et al.*, Phys. Rev. Lett. **119**, 044802 (2017).
[36]S. M. Hooker, R. Bartolini, S. P. D. Mangles, A. Tünnermann, L. Corner, J. Limpert, A. Seryi, and R. Walczak, J. Phys. B: At., Mol. Opt. Phys. **47**, 234003 (2014).
[37]S. Cheshkov, T. Tajima, W. Horton, and K. Yokoya, Phys. Rev. Spec. Top. Accel. Beams **3**, 071301 (2000).
[38]K. Nakajima, A. Deng, X. Zhang, B. Shen, J. Liu, R. Li, Z. Xu, T. Ostermayr, S. Petrovics, C. Klier *et al.*, Phys. Rev. Spec. Top. Accel. Beams **14**, 091301 (2011).
[39]J. S. Liu, C. Q. Xia, W. T. Wang, H. Y. Lu, C. H. Wang, A. H. Deng, W. T. Li, H. Zhang, X. Y. Liang, Y. X. Leng, X. M. Lu, C. Wang, J. Z. Wang, K. Nakajima, R. X. Li, and Z. Z. Xu, Phys. Rev. Lett. **107**, 035001 (2011).
[40]B. Newberger, T. Tajima, F. R. Huson, W. Mackay, B. C. Covington, J. R. Payne, Z. Zou, N. Mahale, and S. Ohnuma *Proceedings of the 1989 IEEE Accelerator Science and Technology* (IEEE, 1989), pp. 630–632.
[41]B. S. Newberger and T. Tajima, Phys. Rev. A **40**, 6897 (1989).
[42]T. Tajima, N. K. Mahale, W. W. MacKay, F. R. Huson, S. Ohnuma, B. C. Covington, J. Payne, and B. S. Newberger, Part. Accel. **32**, 235 (1989).
[43]E. A. Peralta, K. Soong, R. J. England, E. R. Colby, Z. Wu, B. Montazeri, C. McGuinness, J. McNeur, K. J. Leedle, D. Walz *et al.*, Nature **503**, 91 (2013).
[44]D. Kawahito and Y. Kishimoto, Phys. Plasmas **24**, 103105 (2017).
[45]Q. Su and J. H. Eberly, J. Opt. Soc. Am. B **7**, 564 (1990).
[46]G. W. Bryant, E. Waks, and J. R. Krenn, Opt. Photonics News **25**, 50 (2014).
[47]Y. Kojima, Y. Masaki, and F. Kannari, J. Opt. Soc. Am. B **33**, 2437 (2016).
[48]X. Liu, Y. Wang, and E. Potma, Opt. Lett. **36**, 2348 (2011).
[49]A. V. Kildishev, A. Boltasseva, and V. M. Shalaev, Science **339**, 1232009 (2013).
[50]K. Kurihara, F. Kuwashima, O. Morikawa, K. Yamamoto, and M. Tani, Rev. Laser Eng. **45**, 158 (2017).
[51]H. Yasufuku, H. Yoshikawa, M. Kimura, K. Ito, K. Tani, and S. Fukushima, Surf. Interface Anal. **36**, 892 (2004).
[52]S. Ayas, A. Cupallari, and A. Dana, Appl. Phys. Lett. **105**, 221608 (2014).
[53]G. Andonian, D. Stratakis, M. Babzien, S. Barber, M. Fedurin, E. Hemsing, K. Kusche, P. Muggli, B. O'Shea, X. Wei, O. B. Williams, V. Yakimenko, and J. B. Rosenzweig, Phys. Rev. Lett. **108**, 244801 (2012).
[54]B. D. O'Shea, G. Andonian, S. K. Barber, K. L. Fitzmorris, S. Hakimi, J. Harrison, P. D. Hoang, M. J. Hogan, B. Naranjo, O. B. Williams, V. Yakimenko, and J. B. Rosenzweig, Nat. Commun. **7**, 12763 (2016).
[55]T. N. Huan, R. T. Jane, A. Benayad, L. Guetaz, P. D. Tran, and V. Artero, Energy Env. Sci. **9**, 940 (2016).
[56]T. R. Simmons, G. Berggren, M. Bacchi, M. Fontecave, and V. Artero, Coord. Chem. Rev. **270–271**, 127 (2014).
[57]D. Brazzolotto, M. Gennari, N. Queyriaux, T. R. Simmons, J. Pécaut, S. Demeshko, F. Meyer, M. Orio, V. Artero, and C. Duboc, Nat. Chem. **8**, 1054 (2016).
[58]N. Kaeffer, A. Morozan, J. Fize, E. Martinez, L. Guetaz, and V. Artero, ACS Catal. **6**, 3727 (2016).
[59]Y. M. Shin, Appl. Phys. Lett. **105**, 114106 (2014).
[60]B. S. Wettervik, A. Gonoskov, and M. Marklund, Phys. Plasmas **25**(1), 013107 (2018).